Schwaighofer, E.; Clemens, H.; Lindemann, J.; Stark, A.; Mayer, S.:

**Hot-working behavior of an advanced intermetallic multi-phase Gamma-TiAl based alloy**

In: Materials Science and Engineering A (2014) Elsevier

DOI: 10.1016/j.msea.2014.07.040

# Hot-working behavior of an advanced intermetallic multi-phase γ-TiAl based alloy

Emanuel Schwaighofer [a,*], Helmut Clemens [a], Janny Lindemann [b,c], Andreas Stark [d], Svea Mayer [a]

[a] Department of Physical Metallurgy and Materials Testing, Montanuniversität Leoben, Roseggerstr. 12, A-8700 Leoben, Austria

[b] Chair of Physical Metallurgy and Materials Technology, Brandenburg University of Technology, Konrad-Wachsmann-Allee 17, D-03046 Cottbus, Germany

[c] GfE Fremat GmbH, Lessingstr. 41, D-09599 Freiberg, Germany

[d] Institute of Materials Research, Helmholtz-Zentrum Geesthacht, Max-Planck-Str. 1, D-21502 Geesthacht, Germany

[*] Corresponding author. Tel.: +43 3842 4024204; fax: +43 3842 4024202.

E-mail address: emanuel.schwaighofer@unileoben.ac.at (E. Schwaighofer).

***Keywords:***

A. synchrotron X-ray diffraction; B. intermetallics; C. thermomechanical processing; D. recrystallization; failure;

***Highlights:***

- Microstructure and phase evolution of a β-solidifying Ti-43Al-4Nb-1Mo-0.1B alloy with minor C and Si
- Deformation study within a temperature range of 1150-1300 °C and a strain rate regime of 0.005-0.5 $s^{-1}$
- Strain-resolved constitutive modeling of the flow behavior up to a true deformation of 0.9
- Surface fitting approach of flow curve data via a hyperbolic-sine law
- Processing maps in correlation with metallographic post-analysis
- Complementary information, i.e. phase fractions and texture, from *in situ* HEXRD experiments
- Critical discussion of experimental difficulties in performing hot-deformation tests

**ABSTRACT**

New high-performance engine concepts for aerospace and automotive application enforce the development of lightweight γ-TiAl based alloys with increased high-temperature capability above 750 °C. Besides an increased creep resistance, the alloy system must exhibit sufficient hot-workability. Therefore, a refined β-solidifying TNM alloy with an alloy composition of Ti-43Al-4Nb-1Mo-0.1B (in at.%) and minor additions of C and Si is investigated by means of uniaxial compressive hot-deformation tests. The occurring mechanisms during hot-working were decoded by ensuing constitutive modeling of the flow curves by a phase field region-specific surface fitting approach via a hyperbolic-sine law as well as by evaluation via processing maps combined with microstructural post-analysis. Furthermore, complementary *in situ* high energy X-ray diffraction experiments give a deeper insight about the deformation behavior of the alloy, i.e. phase fractions and texture evolution during isothermal and non-isothermal compression.

## 1. Introduction

Intermetallic multi-phase γ-TiAl based alloys are used in advanced high-performance combustion engines due to their low density of 3.8 - 4.1 g/cm$^3$ as well as excellent mechanical and oxidation properties at elevated temperatures [1–3]. In particular, β-solidifying γ-TiAl based alloys were developed to improve hot-workability [4]. Further alloy and process development was undertaken to lower the content of creep-deteriorating β/$\beta_o$-phase within the microstructure prevailing during service, which lead to the finding of the well-known TNM alloy with a nominal composition of Ti-43.5Al-4Nb-1Mo-0.1B (in at.%) [3,5–7]. Therein, a considerable volume fraction of disordered β-phase (bcc) acts as a “lubricant” to improve the hot-workability of this class of alloys, whereas its ordered counterpart $\beta_o$ with B2-structure only exhibits a minor portion in the final microstructure [5]. In conclusion, TNM alloys possess a balanced mechanical property profile combining enhanced high-temperature strength and creep resistivity up to 750 °C with suitable ductility at temperatures below the brittle-to-ductile transition temperature (BDTT) [3,7]. Based on the TNM alloy design concept, a further refinement of the alloy composition towards enhanced high-temperature capability, i.e. improved yield strength and creep life at elevated temperatures, was conducted by means of alloying minor additions of C and Si. Therein, interstitial C acts as solid solution strengthener as well as strong carbide forming element in order to improve creep properties at elevated temperatures [8–10] as recently shown for C-containing TNM alloys [11]. The formation of ζ-$Ti_5Si_3$ silicides, predominantly at $\alpha_2$/γ-interfaces, additionally improves the creep performance of γ-TiAl based alloys due to enhanced microstructural stability [12–14], whereas lower creep strength can be expected when Si is dissolved in the γ-phase due to preferential

vacancy formation as reported in Ref. [15]. Silicon further improves the oxidation resistance [16,17]. Nevertheless, current creep-optimized TiAl alloys, as the so-called TNB alloys [2,18], suffer from poor workability [19,20], wherefore this type of alloys are more designated for powder metallurgical production processes or isothermal forging operations of hot-worked ingots [21]. As a consequence, besides the modification of the chemical composition a microstructural optimization with respect to grain refinement is the key factor to ensure a reduced tendency of brittle failure and, therefore, sufficient damage tolerance below the BDTT [22–24].

Sellars and McTegart [25] developed a hyperbolic-sine Arrhenius-type approach for the constitutive description of the hot-deformation behavior as can be derived from flow curves. Therein, the strain rate $\dot{\varepsilon}$ is a function of flow stress $\sigma$ and deformation temperature $T$ according to

$$\dot{\varepsilon} = A \sinh(\alpha\sigma)^n \exp\left(-\frac{Q}{RT}\right), \quad (1)$$

where $A$ is supposed to be a material constant, $\alpha$ is the stress level of Power-law breakdown, $n$ refers to the stress exponent and $Q$ to a cumulative activation energy of all simultaneously occurring phase-specific processes, e.g. work hardening (WH), dynamic recovery (DRV), dynamic recrystallization (DRX), and/or attendant phase transformations [26]. These parameters, however, are supposed to be dependent on the true strain level $\varphi$. Early attempts of constitutive modeling of TiAl alloys were reported in Refs. [27–29], where the hot-working parameters were determined from a set of peak and/or plateau stresses by means of linear fitting methods. Recently, Deng et *al.* [30] have shown a similar procedure for a TNM alloy with a composition of Ti-43Al-4Nb-1Mo-0.1B (in at.%) determining a global activation energy of 584 kJ/mol. Werner et *al.* [31] have extended the evaluation technique in case of TNM alloys to (i) a strain-resolved evolution of hot-working parameters as derived from linear fitting as well as (ii) an additional dependency of $A$ from $\dot{\varepsilon}$ and $T$, which can be used to precisely reconstruct isothermal flow curves independently from experimental difficulties. Within the present work, the strain-resolved evolution of hot-working parameters according to (i) was conducted by means of a surface fitting procedure based on Eq. (1) in dependency of strain and phase field region-specific datasets, i.e. taking into account that hot-deformation takes place in the (α+β) or ($\alpha/\alpha_2$+β/$\beta_o$+γ) phase field region.

A further useful approach to characterize the hot-workability of complex multi-phase alloys is the evaluation by means of processing maps [32–37] in combination with reliable metallographic post-analysis. Processing maps consist of the superposition of a strain-resolved (i) power dissipation map and (ii) instability map, which for example allow the identification of DRX domains and safe deformation regimes. For TiAl

alloys, processing maps were firstly established in a temperature range from 800 to 1300 °C and a strain rate regime of $10^{-4}$ to 10 $s^{-1}$ as reported in Ref. [38]. Further works on β-solidifying high Nb-containing TiAl alloys are reported in Refs. [39,40]. According to the dynamic material model, the total power $P = \sigma\dot{\varepsilon}$ absorbed during hot-working can be expressed as

$$P = G + J = \int_0^{\dot{\varepsilon}} \sigma \, d\dot{\varepsilon} + \int_0^{\sigma} \dot{\varepsilon} \, d\sigma, \tag{2}$$

where *G* is the work function and *J* is the power co-content, which is supposed to be related to metallurgical changes [34,41]. From the ratio of *J* and $J_{max} = P / 2$ the efficiency of power dissipation *η* is given by

$$\eta = \frac{J}{J_{max}} = \frac{P-G}{P/2}, \tag{3}$$

where *η* can take values between 0 and 1. *G* can be determined after the modified relation reported in Refs. [42,43], where

$$G = \left[\frac{\sigma\dot{\varepsilon}}{m+1}\right]_{\dot{\varepsilon}_{min}} + \int_{\dot{\varepsilon}_{min}}^{\dot{\varepsilon}} \sigma \, d\dot{\varepsilon}. \tag{4}$$

Therein, the first term is introduced to estimate the *G*-content until the minimum applied strain rate $\dot{\varepsilon}_{min}$, which per definition has to be located within the Power-law regime. Therein, *m* is the strain rate sensitivity or the so-called power partitioning factor, which is defined as

$$m = \frac{\partial J}{\partial G} = \frac{\partial(\log\sigma)}{\partial(\log\dot{\varepsilon})} \approx \frac{\Delta(\log\sigma)}{\Delta(\log\dot{\varepsilon})}. \tag{5}$$

The determination of *G* according to Eq. (4) is not only limited to Power-law behavior (dislocation climb alone as dominating mechanism), but also applicable to Power-law breakdown (dislocation climb and glide) [44]. As a generally valid instability criterion the *D* = *J* condition is used [37], where the power dissipation function *D* is set equal to metallurgical changes. Thereafter, unstable flow is expected to occur when [41]

$$\frac{2m}{\eta} - 1 < 0. \tag{6}$$

Complementary *in situ* high energy X-ray diffraction (HEXRD) experiments were performed as reported in Refs. [45,46] in order to extent knowledge on, e.g., phase evolution and texture development. *In situ* methods are not restricted to microstructural post-analysis and give a deeper view of the mechanisms occurring during hot-deformation and, additionally, allow identifying difficulties within test execution. *In situ* HEXRD deformation experiments also allow a phase-specific evaluation of the mechanisms arising from

deformation within the different phase field regions as reported in Refs. [45,47]. The results from constitutive modeling and processing maps enable the design of tailored *in situ* HEXRD hot-deformation experiments.

## 2. Materials and experimental

The refined TNM material with a chemical composition of Ti-42.82Al-4.05Nb-1.01Mo-0.11B (in at.%) and small additions of C and Si (C + Si ≤ 1 at.%) was produced by GfE Metalle und Materialien GmbH, Nuremberg, Germany, by single vacuum arc remelting (VAR) of a powder metallurgically compacted electrode and centrifugal casting subsequent to vacuum induction melting (VIM) in a skull melter [3]. The cast material was subjected to hot-isostatic pressing (HIP) for 4 hours at 1200 °C with following furnace cooling.

In order to study the hot-working behavior of the cast/HIP TNM material and to record the corresponding flow stress versus strain curves uniaxial hot-compression tests were performed with a Gleeble® 3500 device. Thereby, samples with a diameter of 10 mm and a length of 15 mm were heated conductively with 300 K/min to the temperature of interest to prevent from temperature-overshoot and held for 5 min to adjust a materials condition close to thermodynamic equilibrium. Then, the samples were deformed isothermally at temperatures between 1150 and 1300 °C up to a true strain $\varphi$ of 0.9, which corresponds to a height reduction of 60 %, using strain rates in the range of 0.005-0.5 $s^{-1}$. The temperature was controlled by means of type S thermocouples spot-welded directly on the sample surface. The deformation tests were conducted under vacuum atmosphere with a pressure of $10^{-4}$ mbar. After the isothermal deformation sequence the samples were cooled to room temperature (RT) with a rate of ~ 200 K/min.

The preparation of the initial and deformed microstructures was performed by means of standard metallographic methods according to [48]. The evaluation of microstructural constituents was conducted according to the approach reported in [24]. The samples were vibrational or electrolytical polished previous to the investigation in the scanning electron microscope (SEM) performed in back-scattered electron (BSE) mode with a FE-REM MIRA from Tescan, Czech Republic, or an EVO 50 from Zeiss, Germany. Microstructural post-analysis was carried out in the center area, whereas the evaluation of instabilities was applied close to the fringe zone of the deformed samples.

For constitutive description of the flow behavior, the strain-resolved datasets $\sigma = f(T,\dot{\varepsilon})$ were fitted with a rearranged surface function based on the sinh-approach according to Eq. (1). Therefore, the fitting procedure was conducted with the software package Origin 8.5 from OriginLab, USA, within the

characteristic phase field regions ($\alpha/\alpha_2+\beta/\beta_o+\gamma$) and ($\alpha+\beta$). Processing maps according to Eqs. (2-6) were also generated with Origin 8.5.

*In situ* HEXRD phase evolution experiments were carried out as reported in Ref. [11] in order to investigate the development of phase fractions as a function of temperature. To this end, the temperature was corrected by means of heat treatments with calibrated type S thermocouples for 1 h below the γ-solvus temperature ($T_{\gamma solv}$), i.e. the temperature where the γ-phase is dissolved in the matrix, followed by water quenching and quantitative metallographic post-analysis [11,49].

Complementary to the Gleeble compression tests, *in situ* HEXRD deformation experiments with a modified quenching and deformation dilatometer DIL 805 A/D [50] from Bähr Thermoanalyse GmbH, Germany, were executed at the synchrotron facility DESY in Hamburg, Germany, with a photon energy of 100 keV and a beam cross-section of 0.8·0.8 $mm^2$. Therein, samples with 5 mm in diameter and 10 mm in length were heated under Ar-Atmosphere with 400 K/min to annealing temperature by means of a widened water-cooled induction coil. Subsequently, the samples were held for 15 min below or 5 min above $T_{\gamma solv}$ to adjust thermodynamic equilibrium. During ensuing deformation the samples were compressed up to a true strain of 0.6, which is equal to a height reduction of about 45 %. Isothermal deformation experiments with a strain rate of 0.005 $s^{-1}$ were performed at the HZG-beamline HARWI II at the Doris II storage ring using a mar555 flat panel detector from Marresearch GmbH, Germany, according to Ref. [51]. Additionally, non-isothermal deformation experiments were carried out at the HZG-operated beamline HEMS at Petra III with a Perkin Elmer XRD 1622 flat panel detector [52]. Therein, starting from the ($\alpha+\beta$) phase field region the temperature was deliberately decreased during the compression sequence with ~ 2 K/s by applying a strain rate of 0.005 or 0.025 $s^{-1}$. After deformation the samples were quenched with a cooling rate of > 50 K/s to 600 °C followed by 150-200 K/min to RT. The raw data were processed with the software Fit2D [53]. Further details referring the evaluation method are given in Ref. [46]. For the used experimental setup the loading direction (LD) is parallel to the detector plane allowing the investigation of strain-resolved texture evolution [51]. Further details on the experimental environment are reported in Refs. [51,52]. Texture analysis was performed from the two-dimensional diffraction patterns by means of a 2D-Rietveld fitting approach with the software MAUD applying an azimuthal resolution of 5° as described in [54,55]. The static implementation of the dilatometer table makes the realization of grain tracking experiments impossible as presented in Ref. [47].

## 3. Results and discussion

### 3.1 Initial microstructure and refined TNM alloy system

At RT TNM alloys consist predominantly of the three major phases γ-TiAl ($L1_0$-structure), $\alpha_2$-$Ti_3Al$ ($D0_{19}$-structure) and $\beta_o$-TiAl (B2-structure), whereas the disordered counterpart phases α-Ti(Al) (A3-structure) and β-Ti(Al) (A2-structure) are thermodynamically stable above their ordering temperatures. The cast/HIP microstructure shown in Fig. 1 is the initial microstructure prior to the hot-deformation experiments. Therein, 75 vol.% $\alpha_2$/γ-colonies with a γ-lath thickness of ~ 1 µm are surrounded by about 7 vol.% $\beta_o$-phase, which contains $\omega_o$-precipitations ($B8_2$-structure) [56] and 17 vol.% of globular γ-grains (Fig. 1a). The addition of Si causes the formation of < 1 vol.% ζ-$Ti_5Si_3$ silicides with a size of ~ 1 µm as depicted in Fig. 1b. After HIPing the content of C is completely dissolved within the $\alpha_2$- and γ-phase, which agrees well with the investigations reported in Ref. [11]. A residual phase content of 1 vol.% can be attributed to secondary $\beta_o$-precipitates, which are precipitated within the $\alpha_2$/γ-colonies.

The evolution of phase fractions of the TNM-C-Si alloy as determined by *in situ* HEXRD experiments is given in Fig. 2. Therein, during heating from 1100 to 1300 °C with 2 K/min the $\alpha_2$-phase begins to disorder at 1175 °C, which refers to the eutectoid temperature $T_{eut}$. At 1200 °C the disordering reaction of the $\alpha_2$-phase is finished. The disordering range of the $\beta_o$-phase lasts from 1205 to 1230 °C. $T_{\gamma solv}$ was determined to be 1260 °C. Accelerated heating at 1300 °C with 15 K/min to reduce accompanied grain growth enabled the determination of the β-transus temperature $T_\beta$ to be 1450 °C. Thus, Fig. 2 is in good agreement with the TNM-C phase diagram as reported in [11] and shows a minimum of the β-phase in the vicinity of $T_{\gamma solv}$ as typical for TNM alloys [3,5]. Nevertheless, alloying with C yields to (i) an enhanced content of α/$\alpha_2$-phase, (ii) increased ordering temperatures of α- and β-phase, as well as (iii) a $T_\beta$ which is higher when compared to the C- and Si-free TNM alloys investigated in Refs. [24,49]. However, $T_{\gamma solv}$ stays nearly constant. The addition of Si (as well as a reduced content of Al) promotes the stabilization of the β-phase as reported in Ref. [57]. Throughout the performed *in situ* HEXRD heating experiment the amount of carbides and/or silicides was below the resolution limit.

### 3.2 Uniaxial compression tests

The experimentally derived flow curves from the isothermal Gleeble tests for 4 different temperatures and 3 different strain rates are shown in Fig. 3. The corresponding microstructures after deformation until $\varphi = 0.9$ are given in Fig. 4. The flow curves within the ($\alpha/\alpha_2+\beta/\beta_o+\gamma$) phase field region show a pronounced stress peak before an almost “steady state” plateau is reached, whereas the curves obtained within the (α+β)

phase field region nearly follow a constant stress level. Commonly, a stress peak is related to DRX, where the peak marks the onset of DRX as a consequence of a critical defect density arising from WH, i.e. $\varphi = 0.05 - 0.1$ in Fig. 3, while the absence of a peak is often understood that DRV is the dominating mechanism during hot-working [58]. This fact is partially true for multi-phase compounds due to multiple occurring deformation mechanisms and interactions between the phases. In a materials-independent view, a peak or sharp maximum of the flow behavior is primarily attributed to flow localization within the sample material, whereas a steady course of the flow curve can be understood as a uniform deformation [58,59]. From the flow curves displayed in Fig. 3 it is also evident that the flow stress increases with decreasing temperature and increasing strain rate, where the effect is stronger within the ($\alpha/\alpha_2+\beta/\beta_o+\gamma$) phase field region than within the ($\alpha+\beta$) phase field region.

Depending on the specific phase field region where hot-deformation has taken place the microstructures possess different characteristic features (see Fig. 4). Deformation within the ($\alpha/\alpha_2+\beta/\beta_o+\gamma$) phase field region leads to heavily deformed $\alpha_2/\gamma$-colonies featuring bent lamellae. Around the $\alpha_2/\gamma$-colonies the deformation is localized building a necklace structure, which consists of fine-grained DRX γ-grains. The volume fraction of necklace structure and the size of the corresponding recrystallized γ-grains increase with deformation time, i.e. decreasing strain rate, and temperatures up to 1200 °C. Additionally, the $\alpha_2/\gamma$-colonies are surrounded by $\beta_o$-phase which can appear either elongated at fast deformation speed or spherodized when the deformation rate is slow. The same behavior of the β-phase is observed after deformation within the ($\alpha+\beta$) phase field region. There, no γ-phase is present during the deformation sequence, wherefore the α-phase is dynamically recrystallized to globular α-grains. Thereby, the β-phase acts as a “lubricant”, i.e. facilitates the deformation accommodation between α-grains [3], and, additionally, triggers the nucleation and growth of α-nuclei during DRX. Minor amounts of h-type carbides and/or ζ-silicides are assumed to promote DRX of the α-phase by means of particle-stimulated nucleation (PSN). Furthermore, the cooling rate of 200 K/min after isothermal deformation leads to the formation of lens-shaped γ-grains within the $\beta/\beta_o$-phase when cooling from the ($\alpha+\beta$) phase field region or possibly to the growth of recrystallized γ-grains when cooling starts from the ($\alpha/\alpha_2+\beta/\beta_o+\gamma$) phase field region, whereas additional γ-phase precipitates within the $\alpha_2/\gamma$-colonies [60]. Due to these cooling effects the post mortem evaluation of phase fractions does not correlate with the phase fractions present at the end of the deformation trial. However, growth and precipitation of γ-phase does not influence the size and morphology of the $\alpha_2/\gamma$-colonies.

From the deformed microstructures as shown in Fig. 4 $T_{\gamma solv}$ would be estimated to be lower than 1250 °C, whereas at 0.5 $s^{-1}$ remnant γ-phase is still present (note: no γ-phase is observed at 1250 °C with 0.005 and

0.05 $s^{-1}$). In contrast, the T-calibrated phase evolution in Fig. 2 indicates $T_{\gamma solv}$ to be 1260 °C. These temperature uncertainties may arise either to (i) local deviations in chemical composition [61], and/or (ii) the T-measurement of the Gleeble testing device, i.e. spot-welded thermocouple on the sample surface. However, conductive heating of the sample leads to a homogeneous temperature distribution, inducing a uniform deformation of the samples. A minor influence of adiabatic heating within the applied strain rate regime was corrected by means of temperature readjustment during the experiment.

### 3.3 Constitutive modeling

A rearranged formulation of Eq. (1), i.e. $\sigma = f(\dot{\varepsilon},T)$, was used to comprehensively describe the viscoplastic flow behavior derived from the experimental flow curve data as depicted in Fig. 3. Therefore, sets of $\sigma = f(\dot{\varepsilon},T)$ data at constant strain levels were fitted by means of the derived surface fitting function as exemplarily shown in Fig. 5a for a true strain of 0.2. There, the complete 3×4 matrix, i.e. strain rate × temperature, was fitted neglecting the differences occurring from deformation within the specific phase field regions. With this procedure the whole dataset cannot be described accurately, especially in the strain rate range of 0.005-0.05 $s^{-1}$ and temperature range of 1250-1300 °C. To elude these uncertainties the fitting procedure was applied to the specific phase field region in agreement with the microstructures after deformation as shown in Fig. 4. The result of surface fitting for the separated ($\alpha/\alpha_2+\beta/\beta_o+\gamma$) and ($\alpha+\beta$) phase field regions is given in Fig. 5b. This separation is caused by the different occurring deformation modes. For example in the ($\alpha/\alpha_2+\beta/\beta_o+\gamma$) phase field region lamellar colony packets have to be deformed, whereas in the ($\alpha+\beta$) phase field region disordered α- and β-grains are deformed as expected from the microstructures in Fig. 4. Therein, the transition between the different phase field regions is not clearly defined due to metrological difficulties (see also section 3.2). The fitted surfaces in Fig. 5 underline the good agreement with the conducted sinh-approach. Thereby, strain rates of 0.005 $s^{-1}$ refer to the Power-law regime, whereas the data for 0.5 $s^{-1}$ are located in the Power-law breakdown region. The intermediate dataset for a constant 0.05 $s^{-1}$ is assigned to the transitional zone.

Applying the fitting procedure to different strain-dependent datasets allows the determination of the hot-working parameters $A$, $Q$, $n$, and $\alpha$ as a function of true strain as depicted in Fig. 6. To accomplish the fitting procedure the starting values were set manually to $A = 10^{25}$ $s^{-1}$, $Q$ = 600 kJ/mol, $n$ = 6 and $\alpha$ = 0.002 for true strain levels above 0.02. $A$ and $Q$ from Figs. 6a,b show a course comparable to the flow curves in Fig. 3, i.e. the values increase followed by a continuous drop, but not reaching a distinct plateau value. However, $n$ in Fig. 6c exhibit an inverse behavior and $\alpha$ seems to decrease linearly (Fig. 6d). When comparing the

constitutive analysis of the different phase field regions ($\alpha/\alpha_2+\beta/\beta_o+\gamma$) and ($\alpha+\beta$) the parameters follow a similar course, whereas the constitutive parameters of the ($\alpha+\beta$) phase field region are shifted to lower values. Thereby, $Q$ exhibits a sharp peak below $T_{\gamma solv}$, whereas a broad peak can be determined above $T_{\gamma solv}$. The lower $Q$-values in the ($\alpha+\beta$) phase field region might be attributed to the different partitioning of the occurring phase-specific deformation mechanisms when compared to the ($\alpha/\alpha_2+\beta/\beta_o+\gamma$) phase field region. The maxima of Q correlate with the peak positions of the corresponding flow curves, i.e. within a true strain range of 0.05-0.1 for the ($\alpha/\alpha_2+\beta/\beta_o+\gamma$) and 0.1-0.2 for the ($\alpha+\beta$) phase field region. Independent from the specific phase field regions the plateau values of $n$ are ranging from approximately 3-4.5 as typical for Power-law creep [25,44].

The strain-resolved evolution of $Q$ below $T_{\gamma solv}$ from Fig. 6b can further be compared with that obtained for a C- and Si-free TNM alloy within the ($\alpha/\alpha_2+\beta/\beta_o+\gamma$) phase field region as reported in Ref. [31]. From the comparison, it is evident that the deformation behavior changes through the addition of C and Si. For example the C- and Si-bearing TNM alloy exhibits with a $Q$-maximum of 850 kJ/mol a distinct peak followed by a decrease until 355 kJ/mol at a strain level of 0.9 (Fig. 6b). In contrast, the TNM alloy in Ref. [31] shows a plateau of 720 ±25 kJ/mol when the maximum $Q$-value is reached. A higher $Q$-peak indicates enhanced deformation resistance, whereas lower $Q$-values at a higher degree of deformation let suppose pronounced DRX behavior. Both differences may be primarily attributed to the addition of C and Si, where, e.g., dissolved C leads to strengthening as well as to a reduction of the stacking fault energies (SFE) of both the α- and γ-phase [2]. The $Q$-plateau of the TNM alloy may be caused by an increased contribution of concurrent DRV during DRX [47].

The recalculated flow curves derived from the strain-resolved values in Fig. 6 match very well with the experimentally determined flow data (see Fig. 3). Therefore, the applied surface fitting leads to an adequate reproduction of the plastic flow behavior of the investigated multi-phase alloy system, even if less data points are present. However, classic linear-based fitting methods only provide satisfying results from datasets greater than a 3×3 matrix. It is also obvious that in case of surface fitting a further refinement of $A = f(\dot{\varepsilon},T)$ as used in Ref. [31] is not implicitly needed.

### 3.4 Processing maps

Based on the experimental flow curves given in Fig. 3 power dissipation maps were generated according to Eqs. (2-5) as shown for characteristic strain levels in Fig. 7. Therein, depending on the SFE of the phases different deformation mechanisms can occur as reported in Ref. [35]. Thus, DRX domains predominantly

appear at temperatures of 0.7-0.8·$T_m$ ($T_m$ is the absolute melting temperature) and $\eta$-values of 0.30-0.40 for phases with low SFE or 0.50-0.55 for phases with high SFE. According to [40] the SFE of the $\alpha/\alpha_2$- and $\beta/\beta_o$-phase are high, when compared to the SFE of the γ-phase, which is rather low. Schmoelzer *et al.* [47] reported phase-specific mechanisms during hot-working as obtained from *in situ* HEXRD experiments of a C- and Si-free TNM alloy applying a mean strain rate of 0.0037 $s^{-1}$. There, the $\alpha/\alpha_2$-phase tends to DRX during deformation in the ($\alpha/\alpha_2$+$\beta/\beta_o$+γ) phase field region at 1220 °C, whereas DRV is the dominating mechanism in the (α+β) phase field region at 1300 °C. The $\beta/\beta_o$-phase is considered to undergo DRV, whereas the γ-phase is attributed to both mechanisms (DRX and DRV). For the C- and Si-containing TNM alloy dissolved C reduces the SFE of the $\alpha/\alpha_2$- and γ-phase leading to an enhanced contribution of DRX as validated by the appearance of DRX domains in Fig. 7. The deformation behavior of the $\beta/\beta_o$-phase should be unaffected due to minor C-solubility as reported in [11]. Additionally, the formation of h-type carbides and ζ-silicides in the (α+β) phase field region may promote DRX throughout particle-stimulated nucleation of α-grains. The occurrence of the DRX domains of the $\alpha/\alpha_2$- and γ-phase in Fig. 7 is in good agreement to the deformed microstructures shown in Fig. 4. According to Fig. 7 wedge cracking should occur preferentially in the temperature range of 0.7-0.8·$T_m$ and $\eta > 0.60$ [35], i.e. 1250-1300 °C with 0.2-0.5 $s^{-1}$. The micrographs in Fig. 8 confirm the formation of wedge-type cracks, which are oriented parallel to the surface up to a depth of about 200 µm.

The instability maps derived from the instability criterion given by Eq. (6) are superimposed to the power dissipation maps in Fig. 7. It is evident that instability takes place in the beginning of hot-working in the range of 1150-1200 °C and 0.05-0.5 $s^{-1}$, which corresponds to the stress peaks of the flow curves within the ($\alpha/\alpha_2$+$\beta/\beta_o$+γ) phase field region shown in Fig. 3, i.e. enhanced deformation localization. At true strains larger than 0.2 the instability domain shifts to enhanced strain rates and decreased temperatures until it vanishes at a strain level above ~ 0.6. The evolution of the instability map agrees well with the formation of round-type cavities when compared to the micrographs in Fig. 8. Therefore, the $D = J$ criterion can be used to accurately and reliably describe the formation of voids, except for the microstructural condition after deformation at 1150 °C and 0.005 $s^{-1}$. In contrast, the commonly used Ziegler instability criterion [35,62] was found to be not appropriate to predict cavity formation.

### 3.5 *In situ* HEXRD deformation experiments

From the results of the previous sections *in situ* HEXRD deformation experiments were designed in order to study the hot-working behavior of the C- and Si-containing TNM alloy under safe conditions, i.e. no

instability should occur during isothermal or non-isothermal deformation tests. An isothermal deformation test was conducted at 1200 °C within the ($\alpha/\alpha_2+\beta/\beta_o+\gamma$) phase field region using a strain rate of 0.005 $s^{-1}$ (Fig. 9). There, the derived flow stress curve from the dilatometer experiment (Fig. 9a) fits well to the flow data of the Gleeble tests as given in Fig. 3, although the deformed Gleeble samples are deformed more homogeneously than the dilatometer samples. The reason for that can be found in the adaptation of the heating device. While, the Gleeble samples were heated conductively, resulting in a homogenous temperature distribution, the dilatometer samples are heated inductively in an asymmetric Cu-coil (Note: the asymmetric shape is necessary to lead through the X-ray beam). Furthermore, the colder $Al_2O_3$ deformation punches used in the dilatometer lead to enhanced heat dissipation, i.e. sample material in the vicinity of the deformation punches exhibits an about 50 °C decreased temperature. Thus, a cylindrical Mo-plate with a thickness of 0.1 mm was implemented between the fixed deformation punch and the dilatometer sample. The better inductive heat coupling of Mo when compared to TiAl results in a homogenized temperature distribution within the TiAl sample. As found in pre-studies, for this single-sided mounting of the Mo-plate to the dilatometer sample the irradiated volume remains still within the deformation zone at least until a maximum strain of 0.6 is applied. Before the deformation process is started the phase fractions are close to thermodynamic equilibrium as shown in Fig. 9b for a holding time of 15 min. From Fig. 9b it is also obvious that a shorter holding time of 5 min, as conducted in the Gleeble experiments (Fig. 3), is not sufficient reaching a stationary condition below ~ $T_{\gamma solv}$. Thus, during the Gleeble tests $\alpha(\alpha_2) \rightarrow \gamma$ phase transformations have an additional, but minor, contribution to the course of the flow curve. Although, the surface temperature in Fig. 9a stays nearly constant at 1200 ±2 °C the true temperature of the measuring volume has to be corrected to 1220 °C according to the phase evolution in Fig. 2. At the beginning of deformation the temperature drops due to the improvement of the thermal contact between the sample and deformation punches causing a volatile increase of the high-frequency (HF) power (Fig. 9a). This leads to a decrease of γ-phase from 27 to 21 m.% within the first 30 s of deformation, which is equal to a temperature raise of +10 °C when compared to Fig. 2. Thereafter, the γ-phase content continuously increases to 52 m.% corresponding to a temperature of 1155 °C, whereas the temperature of the control thermocouple on the sample surface remains constant at 1200 °C (Fig. 9a). The reason for the temperature decrease might be found in (i) the changing contact conditions, i.e. thermal conductance, close to the deformation punches, (ii) the axial temperature gradient due to the widened coil and (iii) the increasing sample cross-section during deformation leading to a different inductive heat coupling. At the end of the deformation segment contact problems of the thermocouple due to local sample bulging provoke the occurrence of a HF power pulse initiating a raise of temperature (Fig. 9a),

which leads to a reduction of γ-phase prior to cooling of 4 m.%, correlating to a temperature increase of 15-20 °C (Fig. 9b). During ensuing quenching no significant change of phase fractions took place, which agrees well with the investigations conducted in Refs. [11,49,63]. The texture evolution of the α-phase during deformation is given in the azimuthal angle-time-plot (AT-plot) of the α($10\bar{1}0$)-reflection as depicted in Fig. 9c. There, the α($10\bar{1}0$)-reflection was chosen due to a peak overlap of α(0002) with γ(111) occurring in the ($\alpha/\alpha_2+\beta/\beta_o+\gamma$) phase field region. Therein, the sharp diffraction spots at the beginning of deformation correspond to large grains present in the untextured cast/HIP microstructure [11]. During further deformation the α/γ-colonies rotate, whereby the diffraction spots become diffuse due to plastic deformation. A deformation texture in transversal direction (TD) is formed, where the maximum intensity occurs approximately at a true strain of 0.2-0.3. With increasing amount of γ-phase from 21 to 52 m.% the α($10\bar{1}0$)- or $\alpha_2$($20\bar{2}0$)-reflections are getting spotty again, which possibly can be attributed to existent pixel failures from the used mar555 flat panel detector. The corresponding inverse pole figures (IPFs) at true strains of 0.3 and 0.6 in Fig. 9d agree well with the AT-Plot, i.e. texture sharpness is increased at a true strain of 0.3, and indicate the formation of a diffuse basal fiber texture of the $\alpha/\alpha_2$-phase in loading direction (LD).

An isothermal hot-deformation experiment conducted within the (α+β) phase field region at 1250 °C and a strain rate of 0.005 $s^{-1}$ is shown in Fig. 10. There, the flow stress data in Fig. 10a again correspond well to the flow curves obtained in Fig. 3. Comparing the phase fraction evolution in Fig. 10b with Fig. 2 the true temperature before deformation has to be corrected to about 1305 °C. Note the oscillation of the β-phase content between 10 and 15 m.% during isothermal holding which can be correlated to temperatures of 1275 and 1315 °C, respectively. During deformation the content of β-phase increases from 13 to 22 m.% correlating to a temperature raise up to 1335 °C, which is in good agreement with the isothermal deformation experiment below $T_{\gamma solv}$ (see Fig. 9). At the end of the deformation trial approximately 12 m.% β-phase are present, which is equal to a temperature of 1295 °C. The AT-plot during deformation in Fig. 10c shows again a spotty intensity distribution of α(0002) at the beginning of deformation corresponding to the coarse-grained and untextured cast/HIP microstructure. Subsequent plastic deformation leads to peak broadening due to defect formation and multiplication within the α-phase. Concurrent DRX of the α-phase induces a broad intensity distribution expecting minor texture, which seems to sharpen around LD at the end of deformation (Fig. 10c). The IPFs of the $\alpha/\alpha_2$-phase in Fig. 10d confirm the texture evolution as estimated from the AT-Plot of the α(0002)-reflection. Thus, a weak tilted basal fiber texture of the $\alpha_2$-phase is present in LD after deformation at RT which is the result of DRX of the α-phase. Furthermore, it is obvious that the missing peak of the flow curve cannot be attributed to an enhanced occurrence of DRV as would be interpreted from a

classic flow curve of a single-phase material (compare also micrographs in Fig. 4, where the α-grains apparently show an elongated feature, but consist of recrystallized grains). Immediately before quenching a sudden temperature raise of the control thermocouple can be observed, whereas the HF power remains nearly constant. Thus, the β-phase content may increase before quenching, where the disordered β-phase retransforms to α-phase [11,63]. In Fig. 10b the β-phase content decreases from 12 to 8.m% during quenching.

Finally, a non-isothermal hot-working experiment starting from the (α+β) phase field region at 1300 °C with a constant strain rate of 0.005 $s^{-1}$ was applied. Thereby, the flow stress steadily increases with strain due to raising deformation resistance with decreasing temperature down to the (α/$α_2$+β/$β_o$+γ) phase field region (Fig. 11a). Before deformation starts a fraction of 16 m.% β-phase is present (Fig. 11b), which corresponds to a true temperature of 1320 °C (Fig. 2). During deformation the amount of β-phase decreases continuously to about 10 m.% before the test is terminated. At a corrected temperature of 1255 °C, which is 5 °C below $T_{\gamma solv}$, γ-phase is formed at the expense of α-phase. In contrast, experiments with comparable cooling rates from the (α+β) phase field region without the application of an external load require a supercooling of 150-200 °C until γ-phase formation within $α_2$-grains takes place [60]. Obviously, deformation leads to accelerated precipitation of the γ-phase. During further deformation the temperature drops down to a corrected value of 1140 °C, where 51 m.% γ-phase are precipitated, which is in good agreement with the thermodynamic equilibrium data shown in Fig. 2. Upon quenching at the end of the experiment no change of the phase fractions could be observed. The texture information about the α/$α_2$-phase during deformation is given in Fig. 11c. Because this non-isothermal experiment was conducted at the more brilliant X-ray source Petra III in combination with a faster detector a higher time and space resolution is ensured. For deformation temperatures above $T_{\gamma solv}$ the coarse-grained cast/HIP microstructure is refined by means of DRX of the α-phase. Thereby, the onset of DRX is assigned to a true strain of about 0.15-0.25 where the spotty reflections become diffuse (compare Figs. 11a,c). The weak texture of the α$(10\bar{1}0)$- or $α_2(20\bar{2}0)$-reflections in the (α+β) phase field region sharpens in TD below $T_{\gamma solv}$, which is associated with a change in deformation mode from the deformation of α-grains to α($α_2$)/γ-colonies. A significant texture of the γ-phase initially arises above a critical γ-phase content of about 15 m.%, which should belong to the limit where the deformation mode switches (compare Figs. 11b,d). The microstructure after the experiment depicted in Fig. 11 is given in Fig. 12a exhibiting typical features as compared to isothermal deformation below $T_{\gamma solv}$, e.g. necklace structure and deformed lamellae within the $α_2$/γ-colonies. According to [51,64] the coarse-grained $α_2$/γ-

colonies which are elongated perpendicular to LD lead to a characteristic tilted basal fiber texture of the $\alpha_2$-phase as shown in the corresponding IPF displayed in Fig. 12c.

In comparison, a similar non-isothermal *in situ* HEXRD deformation experiment with a faster strain rate of 0.025 $s^{-1}$ was applied, where deformation up to a true strain of 0.6 is finished above $T_{\gamma solv}$. The corresponding micrograph is given in Fig. 12b showing a significantly refined microstructure when compared to Fig. 12a consisting of residual aligned $\beta_o$-phase and supersaturated recrystallized $\alpha_2$-grains with a median diameter of about 10 µm. Therein, the wavy occurrence of the $\alpha_2$-grains is a typical feature of DRX [35]. The related IPF in Fig. 12d proves that no statistically significant texture exists in the $\alpha_2$-phase. From Fig. 12b it is also evident that PSN promotes DRX due to enhanced nucleation of α-phase at β-phase as well as at ζ-silicides and h-type carbides. Obviously, h-type carbides are formed during deformation due to (i) the lower C-solubility of the disordered α-phase when compared to the ordered $\alpha_2$-phase [60], and (ii) an increased content of β-phase which shows an insignificant solubility for C [11]. However, with the applied exposure times of 0.5-1 s it was not possible to study the carbide formation, which was obviously below the detection limit of the experimental conditions. Therefore, this information is only accessible from post mortem examination.

## 4. Conclusions

The phase evolution of a β-stabilized γ-TiAl based alloy, called TNM alloy, with a nominal composition of Ti-43Al-4Nb-1Mo-0.1B (in at.%) which contains a small amount of C and Si (C + Si ≤ 1 at.%) shows the same characteristic features as a C- and Si-free TNM alloy, i.e. solidification pathway via the β-phase and a minimum of the β-phase in the vicinity of the γ-solvus temperature $T_{\gamma solv}$. However, the TNM-C-Si alloy exhibits increased disordering temperatures of the $\alpha_2$- and $\beta_o$-phase of about 25 °C as well as an increased β-transus temperature $T_\beta$ of about 50 °C. However, $T_{\gamma solv}$ stays nearly constant. Additionally, the formation of ζ-$Ti_5Si_3$ silicides and h-type carbides $Ti_2AlC$ could be observed depending on heat treatment and deformation condition. Deformation studies conducted within a temperature range of 1150 to 1300 °C and a stress rate regime of 0.005 to 0.5 $s^{-1}$ up to a true strain of $\varphi = 0.9$ demonstrate a higher deformation resistance of the TNM-C-Si alloy when compared to the C- and Si-free alloy variant. Depending on the phase field region where deformation takes place, i.e. ($\alpha/\alpha_2+\beta/\beta_o+\gamma$) or (α+β), characteristic microstructural features arise according to the occurring main deformation mechanisms, e.g. bent lamellae within $\alpha_2/\gamma$-colonies and necklace structure of the γ-phase below $T_{\gamma solv}$ as well as dynamically recrystallized (DRX) α-grains above $T_{\gamma solv}$. The improved DRX behavior could be attributed to (i) the lowered stacking fault energies of the $\alpha/\alpha_2$- and γ-phase by C-addition as well as (ii) enhanced particle-stimulated nucleation of α-grains by means of ζ-

silicides and h-type carbides. Thereby, h-type carbides are formed during deformation within the (α+β) phase field region because of a lower C-solubility of the disordered α-phase when compared with the ordered $\alpha_2$-phase as well as an increased volume fraction of β-phase with an insignificant solubility for C. Thus, deformation within the (α+β) phase field region was found to be appropriate for an effective grain refinement of the α-phase, which is a key factor for processing microstructures with improved strength properties and high-temperature capability by maintaining a reduced critical defect size of $\alpha_2$/γ-colonies to prevent from premature failure. Deformation at 1250-1300 °C with 0.005-0.05 $s^{-1}$ and 1200 °C with 0.005 $s^{-1}$ roughly corresponds to the safe hot-working region as evaluated by means of processing maps. There, the power dissipation map could be used to reliably predict phase field region-specific DRX domains of the α- and γ-phase as well as wedge-type cracking, whereas the instability map referred to the formation of round-type cavities, which are predominantly induced at the beginning of plastic deformation. A phase field region-specific constitutive description via a surface fitting approach based on the hyperbolic-sine law also provides satisfying results to reproduce the flow behavior of the C- and Si-bearing TNM alloy. Selected isothermal and non-isothermal *in situ* HEXRD deformation experiments allowed critically discussing experimental difficulties in performing hot-deformation tests in the safe hot-working region, e.g. changing phase amounts and, thus, examination of true temperatures within irradiated sample volume as well as phase-transformational effects during cooling and quenching. The texture evolution during deformation within (α+β) phase field region further confirms the formation of a refined and nearly texture-free microstructure, whereas below a critical amount of about 15 m.% γ-phase the deformation mode changes leading to the formation of undesired coarse-grained and elongated $\alpha_2$/γ-colonies with a significant tilted basal fiber texture of the $\alpha_2$-phase.

**Acknowledgement**

This work was conducted within the framework of the German BMBF project O3X3530A. The support of the DESY management, User Office and HZG beamline staff for performing *in situ* HEXRD experiments at HARWI II, W2 beamline, and HEMS, P07 beamline, is gratefully acknowledged. In particular, the authors thank the beamline scientists Dr. Thomas Lippmann and Dr. Norbert Schell for their assistance. Additionally, these research activities received funding from the European Community's 7th Framework Programme (FP7/2007e2013) under grant agreement no. 226716.

## References


[1] Y.W. Kim, D. Morris, R. Yang, C. Leyens, Structural Aluminides for Elevated Temperature Applications, TMS, Warrendale, 2008.
[2] F. Appel, J.D.H. Paul, M. Oehring, Gamma titanium aluminide alloys: science and technology, Wiley-VCH, Weinheim, 2011.
[3] H. Clemens, S. Mayer, Advanced Engineering Materials 15 (2013) 191.
[4] T. Tetsui, K. Shindo, S. Kobayashi, M. Takeyama, Scripta Materialia 47 (2002) 399.
[5] H. Clemens, W. Wallgram, S. Kremmer, V. Güther, A. Otto, A. Bartels, Advanced Engineering Materials 10 (2008) 707.
[6] H. Clemens, H.F. Chladil, W. Wallgram, G.A. Zickler, R. Gerling, K.D. Liss, S. Kremmer, V. Güther, W. Smarsly, Intermetallics 16 (2008) 827.
[7] W. Wallgram, T. Schmoelzer, L. Cha, G. Das, V. Güther, H. Clemens, International Journal of Materials Research 100 (2009) 1021.
[8] T. Kawabata, M. Tadano, O. Izumi, ISIJ International 31 (1991) 1161.
[9] W.H. Tian, M. Nemoto, Intermetallics 5 (1997) 237.
[10] U. Christoph, F. Appel, R. Wagner, Materials Science and Engineering A 239-240 (1997) 39.
[11] E. Schwaighofer, B. Rashkova, H. Clemens, A. Stark, S. Mayer, Intermetallics 46 (2014) 173.
[12] R. Yu, L.L. He, J.T. Guo, H.Q. Ye, V. Lupinc, Acta Materialia 48 (2000) 3701.
[13] F.-S. Sun, S.-E. Kim, C.-X. Cao, Y.-T. Lee, M.-G. Yan, Scripta Materialia 45 (2001) 383.
[14] H. Zhang, L.L. He, H.Q. Ye, Materials Science and Engineering: A 360 (2003) 415.
[15] X.-W. Du, J.. Wang, J. Zhu, Intermetallics 9 (2001) 745.
[16] K. Maki, M. Shioda, M. Sayashi, T. Shimizu, S. Isobe, Materials Science and Engineering: A 153 (1992) 591.
[17] S. Tsuyama, S. Mitao, K. Minakawa, Materials Science and Engineering: A 153 (1992) 451.
[18] F. Appel, J.D.H. Paul, M. Oehring, H. Clemens, F.-D. Fischer, International Journal of Materials Research 95 (2004) 585.
[19] F. Appel, M. Oehring, R. Wagner, Intermetallics 8 (2000) 1283.
[20] F. Appel, M. Oehring, J.D.H. Paul, C. Klinkenberg, T. Carneiro, Intermetallics 12 (2004) 791.
[21] F. Appel, U. Brossmann, U. Christoph, S. Eggert, P. Janschek, U. Lorenz, J. Müllauer, M. Oehring, J.D.H. Paul, Advanced Engineering Materials 2 (2000) 699.
[22] C. Koeppe, A. Bartels, J. Seeger, H. Mecking, Metallurgical Transactions A 24 (1993) 1795.
[23] Y.-W. Kim, Materials Science and Engineering A 192-193 (1995) 519.
[24] E. Schwaighofer, H. Clemens, S. Mayer, J. Lindemann, J. Klose, W. Smarsly, V. Güther, Intermetallics 44 (2014) 128.
[25] C.M. Sellars, W.J. McTegart, Acta Metallurgica 14 (1966) 1136.
[26] Y.C. Lin, M.-S. Chen, J. Zhong, Computational Materials Science 42 (2008) 470.
[27] M. Nobuki, T. Tsujimoto, ISIJ International 31 (1991) 931.
[28] Z.J. Pu, K.H. Wu, J. Shi, D. Zou, Materials Science and Engineering: A 192-193 (1995) 780.
[29] H.Y. Kim, W.H. Sohn, S.H. Hong, Materials Science and Engineering: A 251 (1998) 216.
[30] Z. Deng, J. Li, T. Zhang, H. Zhong, R. Hu, H. Chang, in:, L. Zhou, H. Chang, Y. Lu, D. Xu (Eds.), Proceedings of the 12th World Conference on Titanium, Science Press, Beijing, China, 2011, pp. 1486–1490.
[31] R. Werner, E. Schwaighofer, M. Schloffer, H. Clemens, J. Lindemann, S. Mayer, Materials Science Forum (2014) in print.
[32] L.E. Malvern, Introduction to the Mechanics of a Continuous Medium, Prentice-Hall, Englewood Cliffs, N.J, 1969.
[33] Y.V.R.K. Prasad, H.L. Gegel, S.M. Doraivelu, J.C. Malas, J.T. Morgan, K.A. Lark, D.R. Barker, Metallurgical Transactions A 15 (1984) 1883.
[34] Y.V.R.K. Prasad, Metallurgical and Materials Transactions A 27 (1996) 235.
[35] Y.V.R.K. Prasad, S. Sasidhara, eds., Hot Working Guide: A Compendium of Processing Maps, ASM International, Materials Park, OH, 1997.
[36] S.V.S. Narayana Murty, B. Nageswara Rao, Journal of Materials Processing Technology 104 (2000) 103.
[37] S.V.S. Narayana Murty, B. Nageswara Rao, B.P. Kashyap, Journal of Materials Processing Technology 166 (2005) 268.
[38] J.H. Kim, Y.W. Chang, C.S. Lee, T. Kwon Ha, Metallurgical and Materials Transactions A 34 (2003) 2165.
[39] G. Wang, L. Xu, Y. Wang, Z. Zheng, Y. Cui, R. Yang, Acta Metallurgica Sinica 47 (2011) 587.
[40] B. Liu, Y. Liu, Y.P. Li, W. Zhang, A. Chiba, Intermetallics 19 (2011) 1184.
[41] S.V.S. Narayana Murty, B. Nageswara Rao, Journal of Materials Science Letters 18 (1999) 1757.
[42] S.V.S. Narayana Murty, B. Nageswara Rao, Journal of Materials Science Letters 17 (1998) 1203.
[43] C. Poletti, H. Dieringa, F. Warchomicka, Materials Science and Engineering: A 516 (2009) 138.
[44] H.J. Frost, M.F. Ashby, Deformation-Mechanism Maps: The Plasticity and Creep of Metals and Ceramics, Pergamon Press, Oxford, New York, 1982.
[45] K.D. Liss, T. Schmoelzer, K. Yan, M. Reid, M. Peel, R. Dippenaar, H. Clemens, Journal of Applied Physics 106 (2009) 1.
[46] T. Schmoelzer, K.-D. Liss, P. Staron, S. Mayer, H. Clemens, Advanced Engineering Materials 13 (2011) 685.
[47] T. Schmoelzer, K.-D. Liss, C. Kirchlechner, S. Mayer, A. Stark, M. Peel, H. Clemens, Intermetallics 39 (2013) 25.
[48] M. Schloffer, T. Schmoelzer, S. Mayer, E. Schwaighofer, G. Hawranek, F.P. Schimansky, F. Pyczak, H. Clemens, Practical Metallography 48 (2011) 594.
[49] M. Schloffer, F. Iqbal, H. Gabrisch, E. Schwaighofer, F.P. Schimansky, S. Mayer, A. Stark, T. Lippmann, M. Göken, F. Pyczak, H. Clemens, Intermetallics 22 (2012) 231.
[50] P. Staron, T. Fischer, T. Lippmann, A. Stark, S. Daneshpour, D. Schnubel, E. Uhlmann, R. Gerstenberger, B. Camin, W. Reimers, E. Eidenberger, H. Clemens, N. Huber, A. Schreyer, Advanced Engineering Materials 13 (2011) 658.
[51] A. Stark, E. Schwaighofer, S. Mayer, H. Clemens, T. Lippmann, L. Lottermoser, A. Schreyer, F. Pyczak, MRS Proceedings 1516 (2013) 71.
[52] E. Schwaighofer, A. Stark, L. Lottermoser, R. Kirchhof, H. Clemens, N. Schell, S. Mayer, in:, HASYLAB Annual Report, HASYLAB/DESY, Hamburg, 2012.
[53] A.P. Hammersley, S.O. Svensson, M. Hanfland, A.N. Fitch, D. Häusermann, High Pressure Research 14 (1996) 235.
[54] I. Lonardelli, H.-R. Wenk, L. Lutterotti, M. Goodwin, Journal of Synchrotron Radiation 12 (2005) 354.
[55] L. Lutterotti, M. Bortolotti, G. Ischia, I. Lonardelli, H.-R. Wenk, Zeitschrift Für Kristallographie Supplements 26 (2007) 125.

[56] M. Schloffer, B. Rashkova, T. Schoeberl, E. Schwaighofer, Z. Zhang, H. Clemens, S. Mayer, Acta Materialia (2014) DOI: 10.1016/j.actamat.2013.10.036.
[57] T. Schmoelzer, S. Mayer, E. Schwaighofer, T. Lippmann, P. Staron, A. Stark, H. Clemens, in:, HASYLAB Annual Report, HASYLAB/DESY, Hamburg, 2010.
[58] G.E. Dieter, D.J. Bacon, Mechanical Metallurgy, McGraw-Hill, London; New York, 1988.
[59] S.L. Semiatin, Formability and Workability of Metals: Plastic Instability and Flow Localization, American Society for Metals, Metals Park, Ohio, 1984.
[60] E. Schwaighofer, H. Clemens, S. Mayer, Unpublished Data 2009 – (2012).
[61] M. Achtermann, V. Guether, J. Klose, H.-P. Nicolai, in:, Presentation at 4th International Workshop on Titanium Aluminides, GfE Metalle und Materialien GmbH, Nuremberg, Germany, 2011.
[62] H. Ziegler, An Introduction to Thermomechanics, 2nd ed., North-Holland Publishing Company, Amsterdam; New York, 1983.
[63] R. Werner, M. Schloffer, E. Schwaighofer, H. Clemens, E. Povoden-Karadeniz, S. Mayer, (2014) in preparation.
[64] A. Stark, A. Bartels, H. Clemens, S. Kremmer, F.P. Schimansky, R. Gerling, Advanced Engineering Materials 11 (2009) 976.

## Figure captions

**Fig. 1**: SEM micrograph of the initial cast/HIP microstructure of the investigated TNM alloy containing small additions of C and Si: a) overview and b) microstructural details in higher magnification. The arrow in b) denotes a bright-contrasted ζ-Ti5Si3 particle.

**Fig. 2**: Temperature-corrected phase evolution of the TNM alloy with small additions of C and Si as determined by *in situ* HEXRD.

**Fig. 3**: Experimentally derived flow stress curves (solid lines) and recalculated true stress-strain curves (■,●,▲,◆) as reported in section 3.3 until a true degree of deformation of $\varphi = 0.9$ within a strain rate regime of 0.005 to 0.5 $s^{-1}$ (a-c) and a temperature range of 1150 to 1300 °C.

**Fig. 4**: Microstructures of the deformed specimens according to the experiments shown in Fig. 3 ($\varphi = 0.9$). In all images the loading direction (LD) is vertical within the image plane.

**Fig. 5**: Fit of deformation data $\sigma = f(T,\dot{\varepsilon})$ by means of a rearranged formulation based on the sinh-law approach according to Eq. (1) at a true degree of deformation of $\varphi = 0.2$: a) fitting of the complete dataset and b) separation of data sets in dependence of the phase field regions ($\alpha/\alpha_2+\beta/\beta_o+\gamma$) and ($\alpha+\beta$).

**Fig. 6**: Strain-resolved evolution of the fitting parameters $A$, $Q$, $n$, and $\alpha$ from the sinh-approach given in Eq. (1) (a-d) in accordance to the fitting procedure depicted in Fig. 5b. Note that the derived parameters were separated corresponding to the occurring phase field regions ($\alpha/\alpha_2+\beta/\beta_o+\gamma$), ▲, and ($\alpha+\beta$), ■.

**Fig. 7**: Strain-resolved processing maps derived from the experimental true stress-strain curves shown in Fig. 3 (see text).

**Fig. 8**: Evolution of instabilities during the deformation experiments given in Fig. 3 ($\varphi = 0.9$): round-type ("r") cavities according to the prediction of the instability map in Fig. 7 and formation of wedge-type ("w") cracks, where $\eta > 60$ %. Thus, the safe deformation region is in the temperature and strain rate range of 1250 to 1300 °C and 0.005 to 0.05 $s^{-1}$, respectively, as well as at 1200 °C and a strain rate of 0.005 $s^{-1}$.

**Fig. 9**: *In situ* HEXRD isothermal deformation experiment within the ($\alpha/\alpha_2+\beta/\beta_o+\gamma$) phase field region at 1200 °C ($T < T_{\gamma solv}$) using a strain rate of 0.005 $s^{-1}$ ($\varphi_{max} = 0.6$): a) dilatometer data, b) phase fractions, c) texture evolution of the $\alpha/\alpha_2$-phase during deformation sequence (AT-plot of $\alpha(10\bar{1}0)$- or $\alpha_2(20\bar{2}0)$-peaks), and d) inverse pole figures (IPFs) of the $\alpha/\alpha_2$-phase in LD at true strains of 0.3 and 0.6 (RT). LD: loading direction; TD: transversal direction.

**Fig. 10**: *In situ* HEXRD isothermal deformation experiment conducted within the ($\alpha+\beta$) phase field region at 1250 °C ($T > T_{\gamma solv}$) with a strain rate of 0.005 $s^{-1}$ ($\varphi_{max} = 0.6$): a) dilatometer data, b) phase fractions, c) texture evolution of α(0002) during deformation, and d) IPFs of the $\alpha/\alpha_2$-phase in LD at true strains of 0.3 and 0.6 (RT).

**Fig. 11**: *In situ* HEXRD non-isothermal deformation experiment with decreasing temperature (~ 2 K/s) from about 1300 to 1100 °C at an applied strain rate of 0.005 $s^{-1}$ ($\varphi = 0.6$): a) dilatometer data, b) phase fractions, and AT-plots during deformation of c) $\alpha(10\bar{1}0)$ or $\alpha_2(20\bar{2}0)$, and d) γ(001).

**Fig. 12**: Deformed microstructures after a) the *in situ* HEXRD experiment conducted in Fig. 11 and b) an identical experiment with an applied strain rate of 0.025 $s^{-1}$, where the final temperature of the deformation trial is above $T_{\gamma solv}$ ($\varphi = 0.6$). IPFs in equal-area projection of the $\alpha_2$-$Ti_3Al$ phase in LD, where c) accords to a) and d) to b), respectively.

Fig_1
Click here to download high resolution image

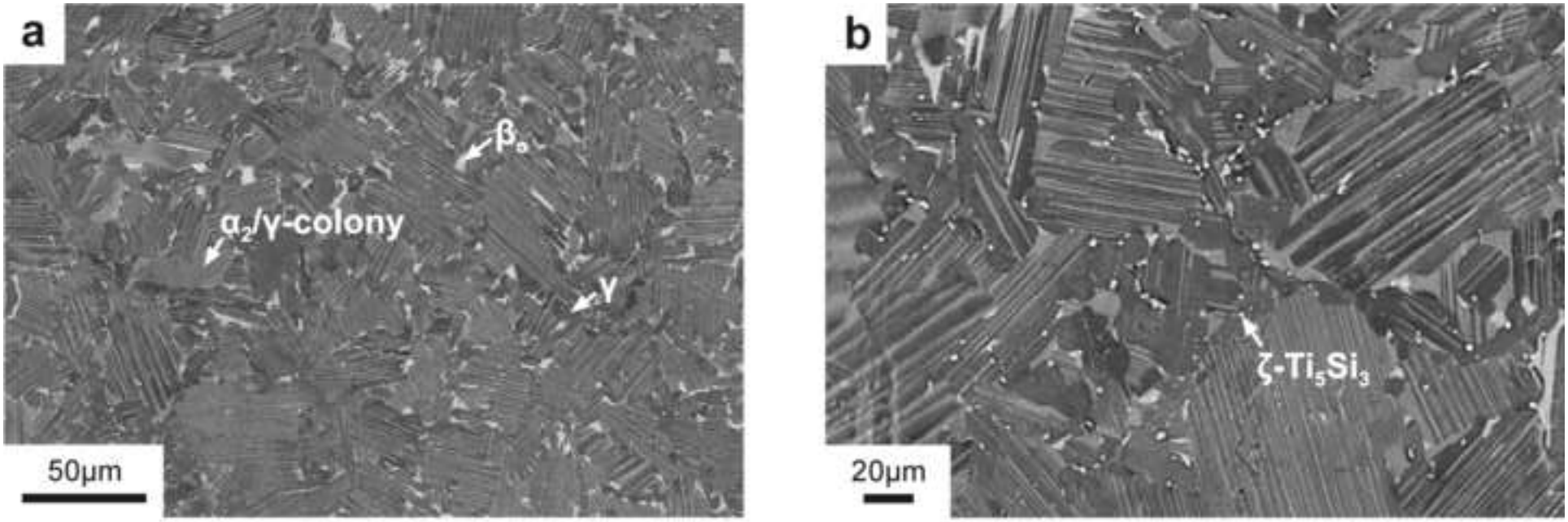

Fig_2
Click here to download high resolution image

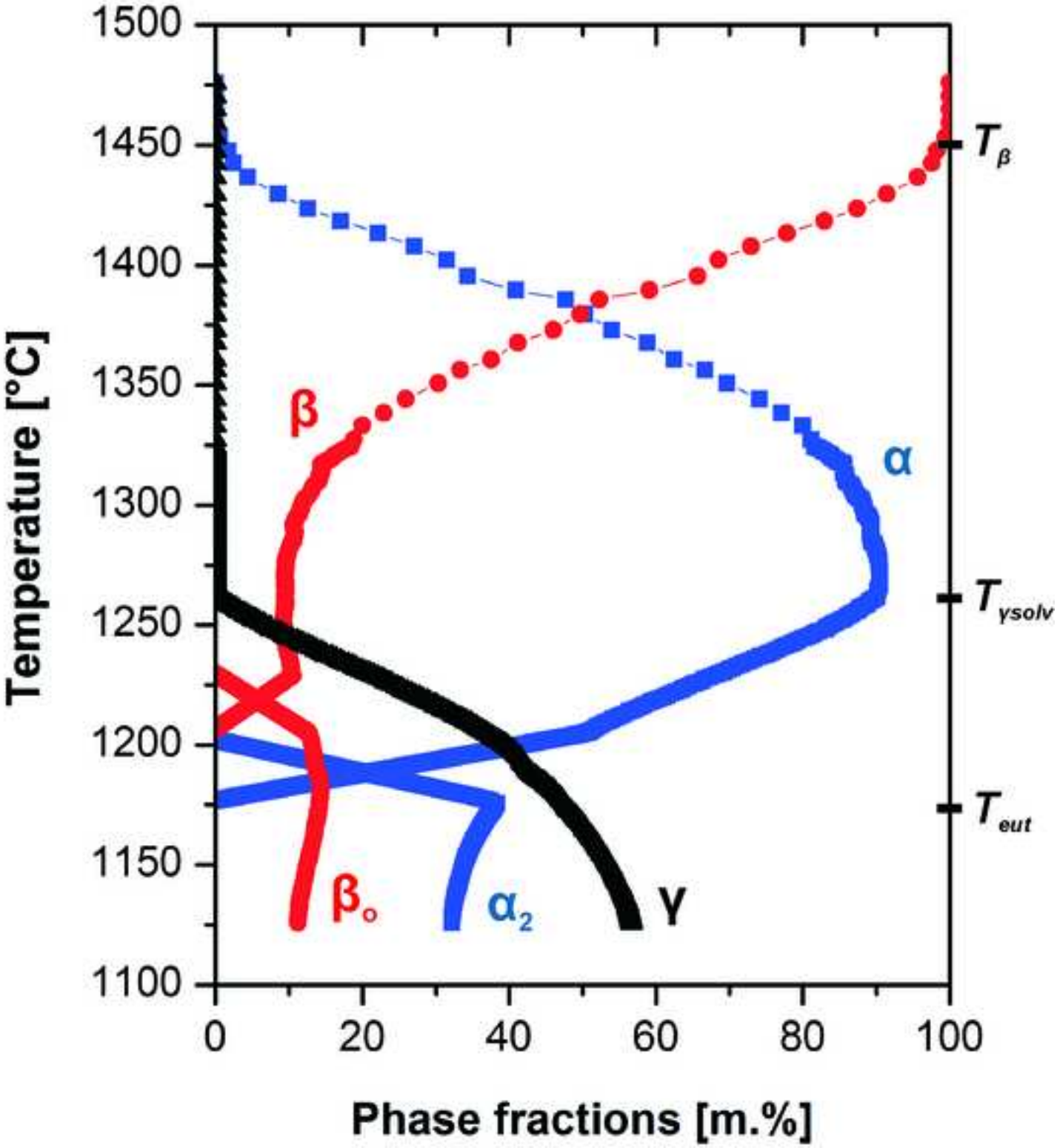

Fig_3

Click here to download high resolution image

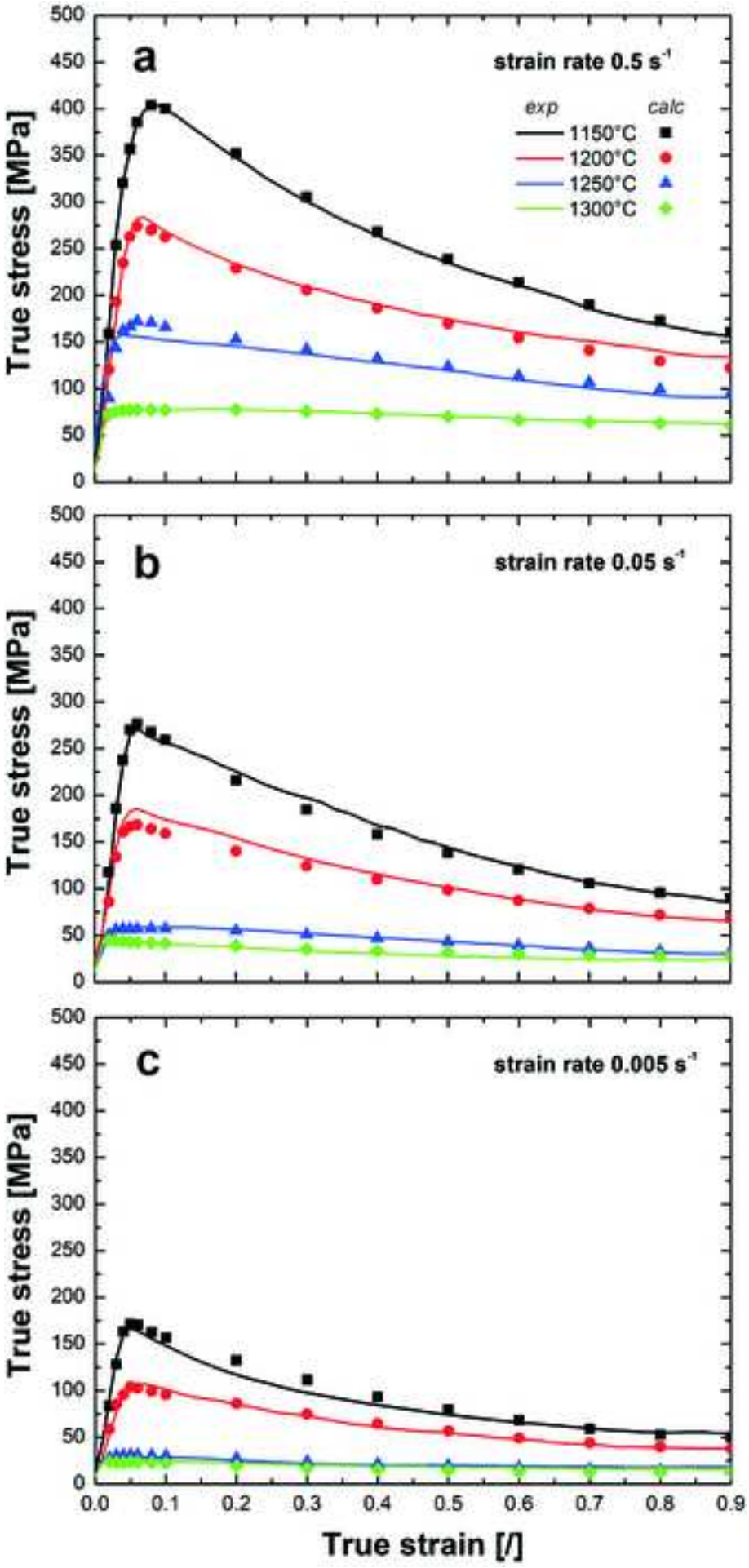

Fig_4

Click here to download high resolution image

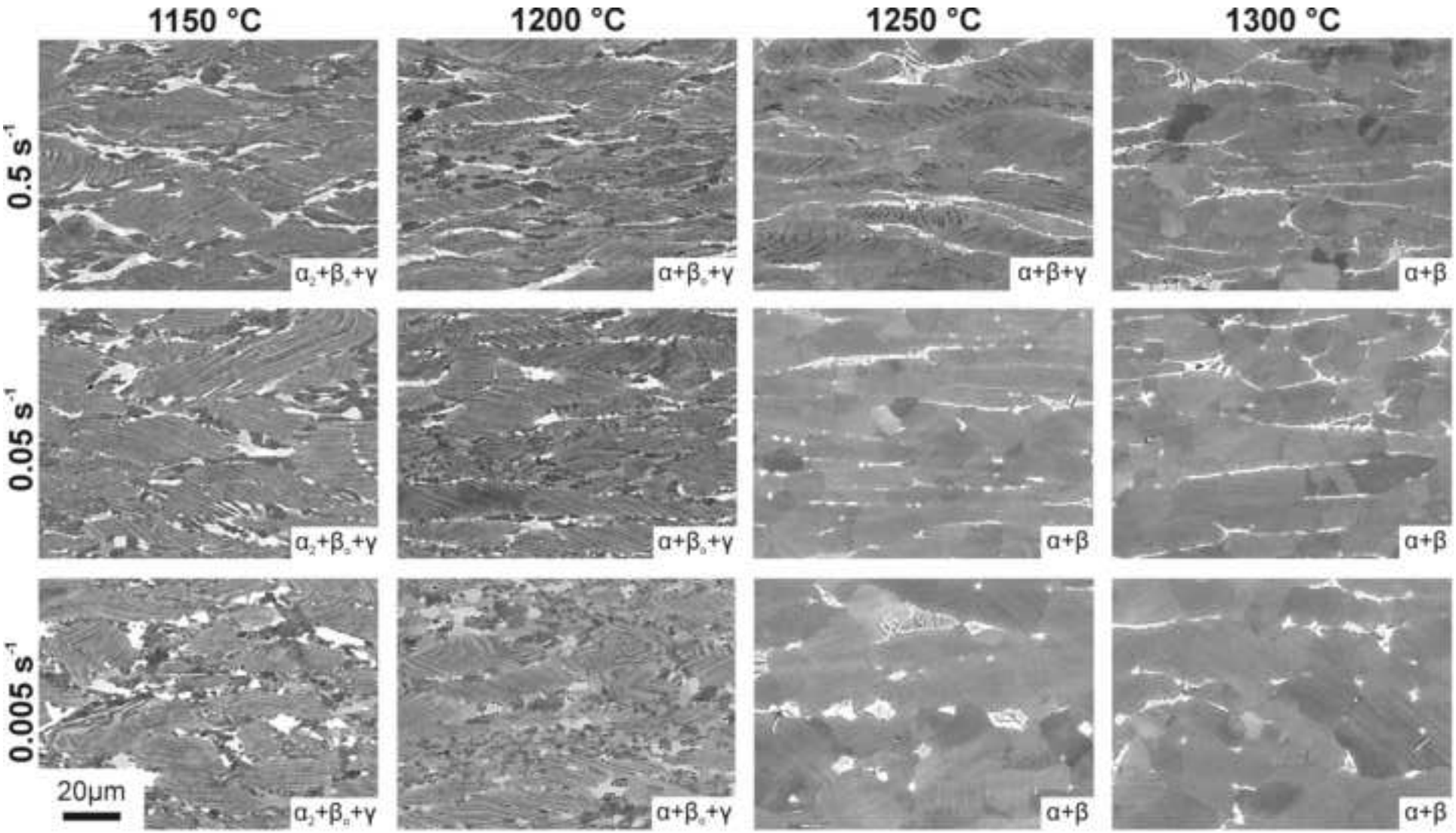

Fig_5

Click here to download high resolution image

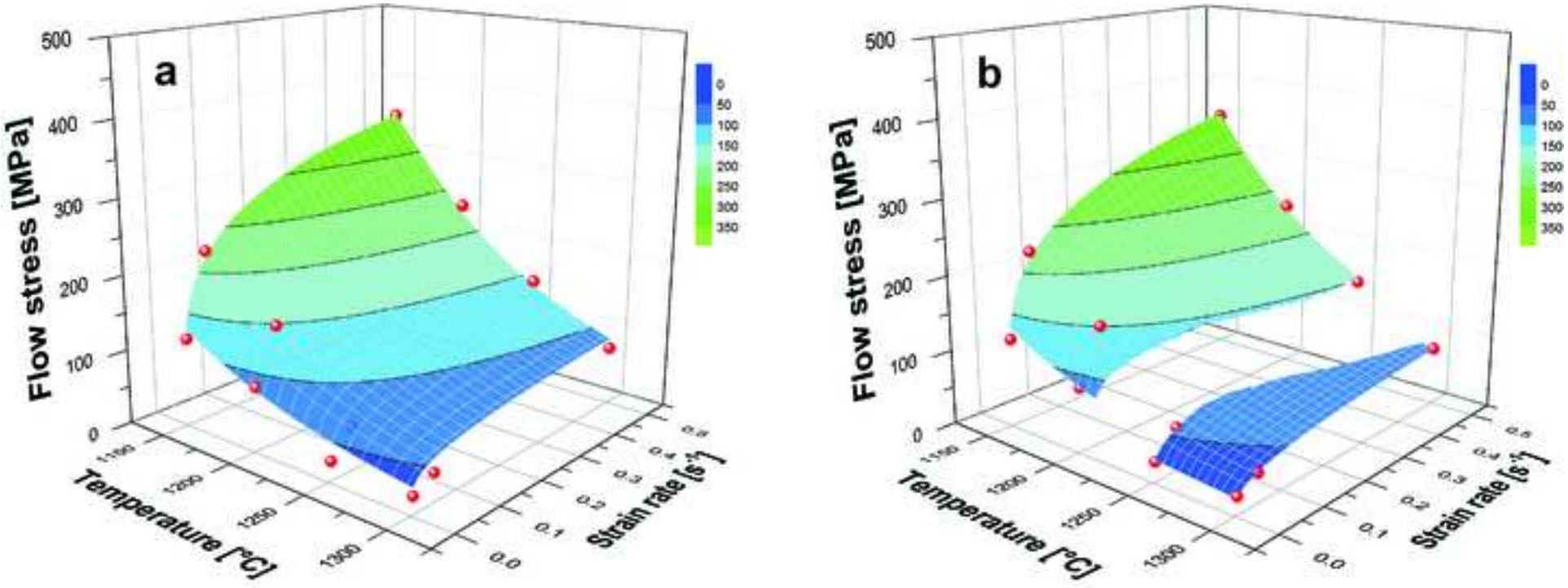

Fig_6

Click here to download high resolution image

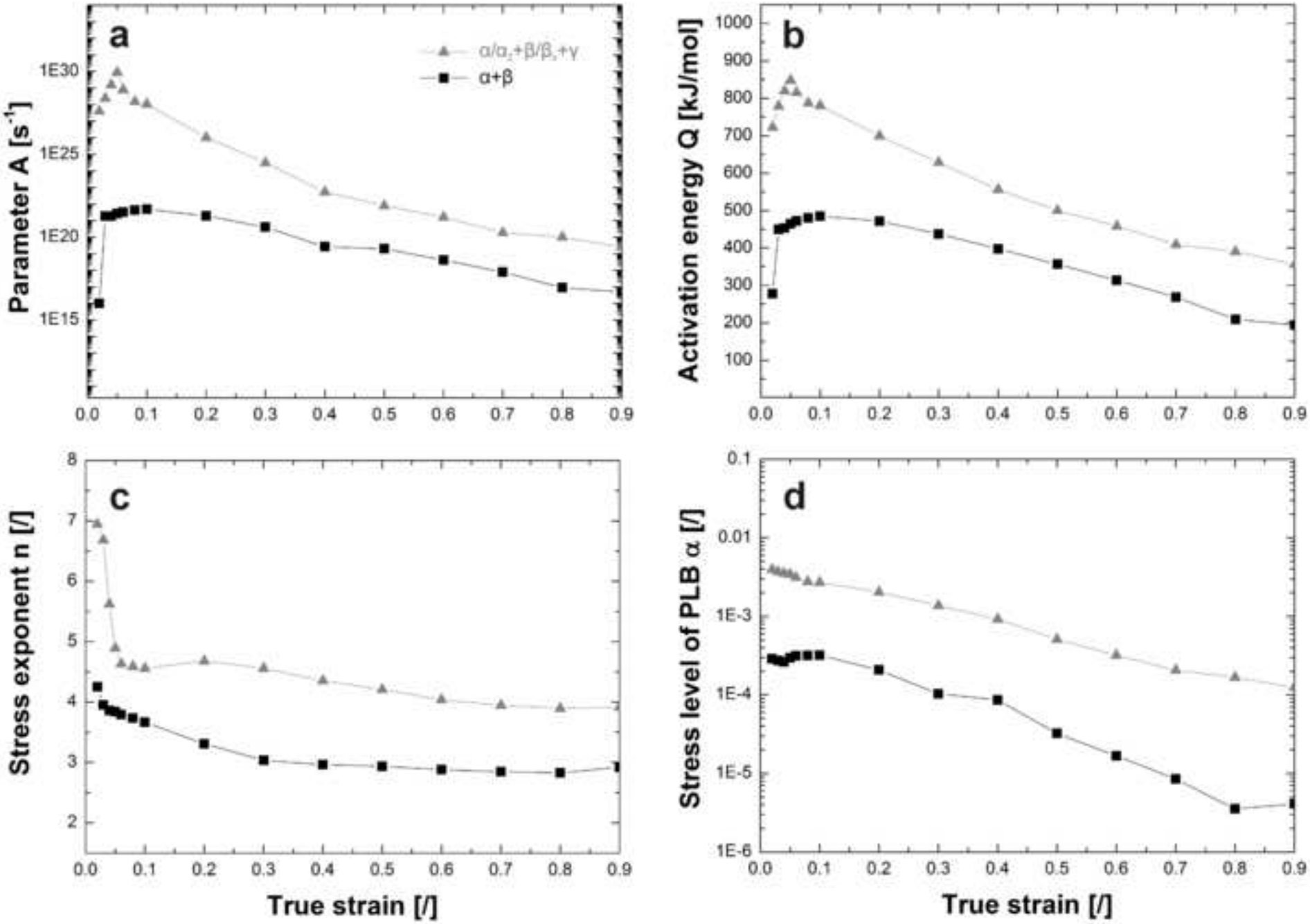

Fig_7

Click here to download high resolution image

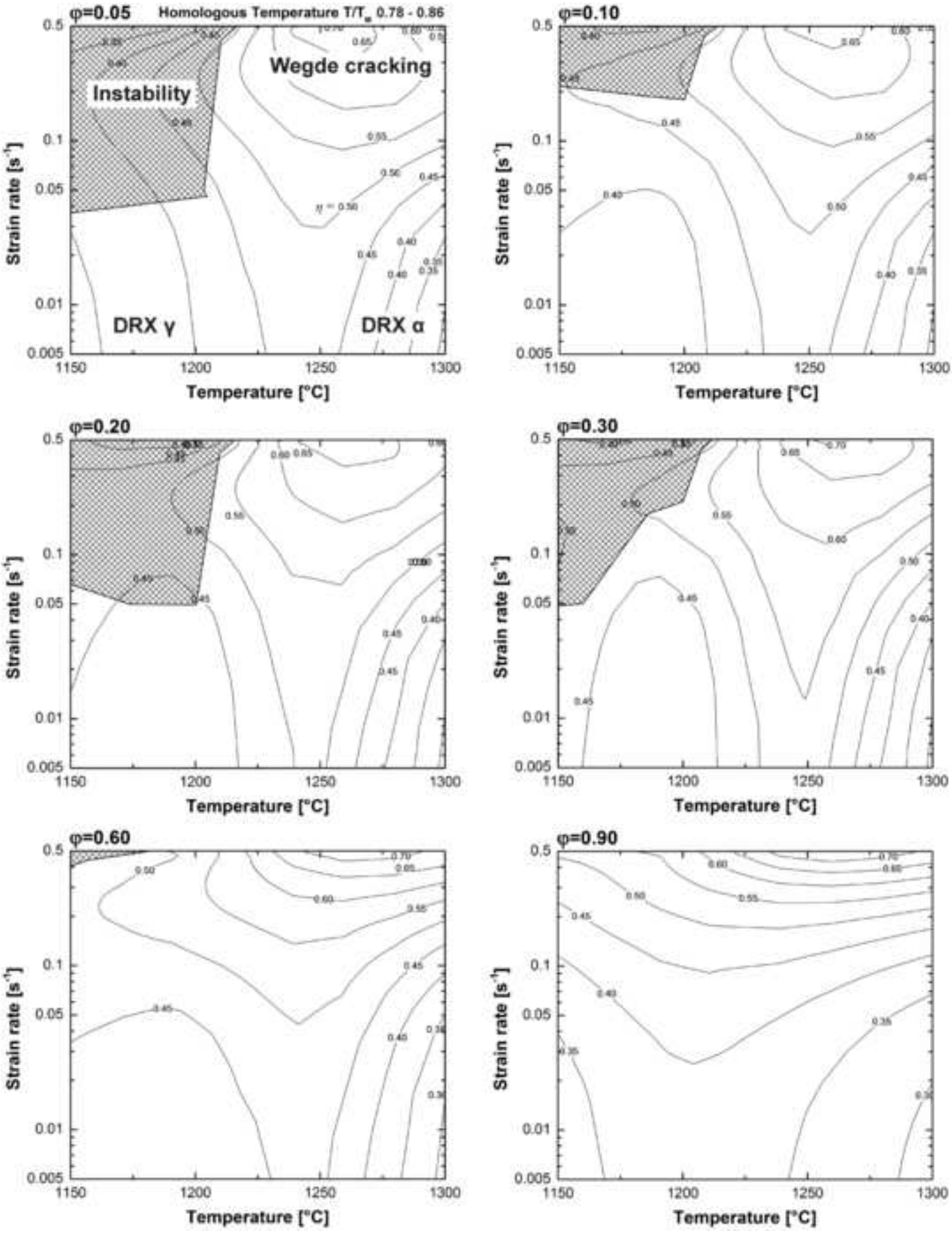

Fig_8

Click here to download high resolution image

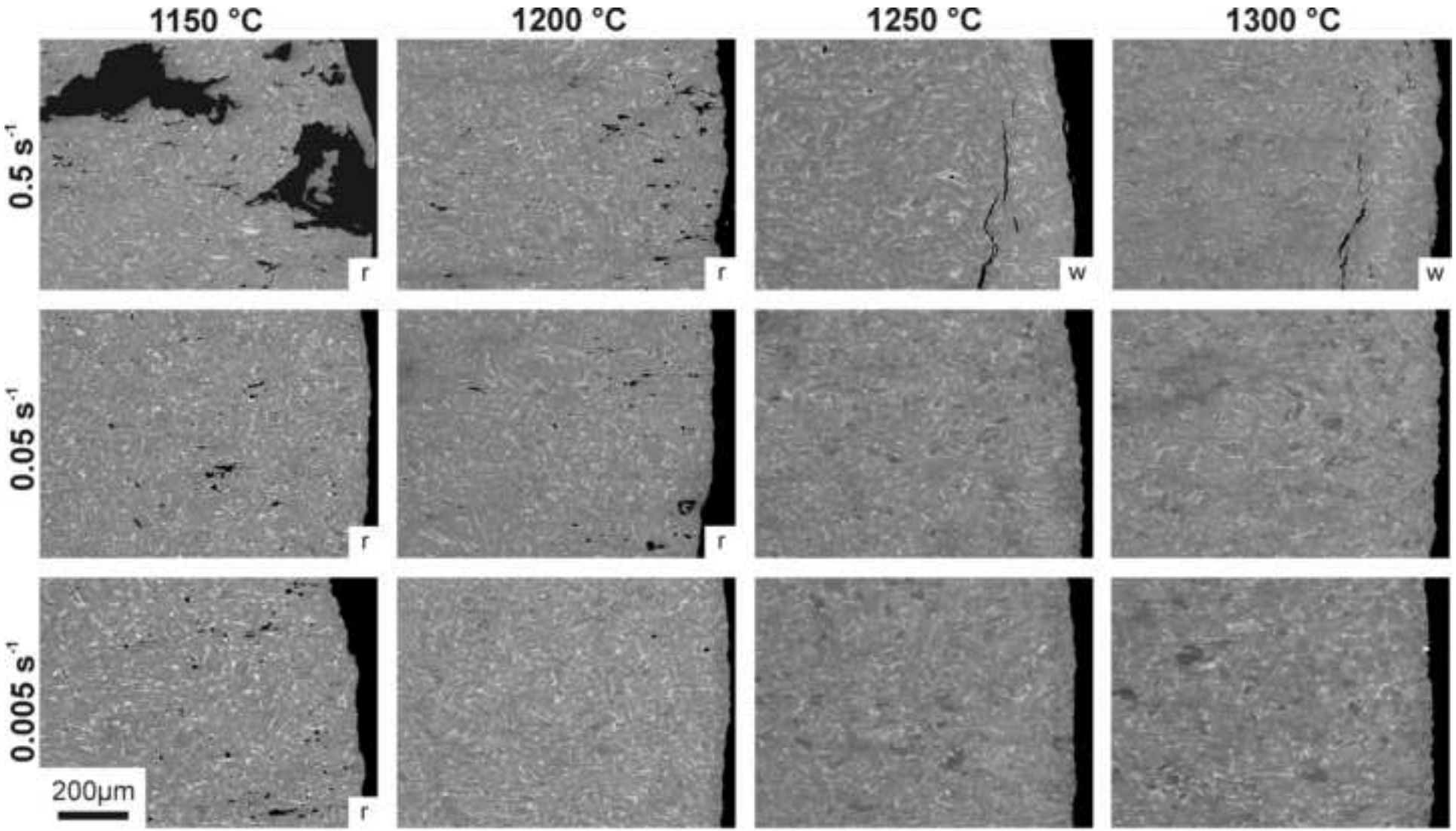

Fig_9

Click here to download high resolution image

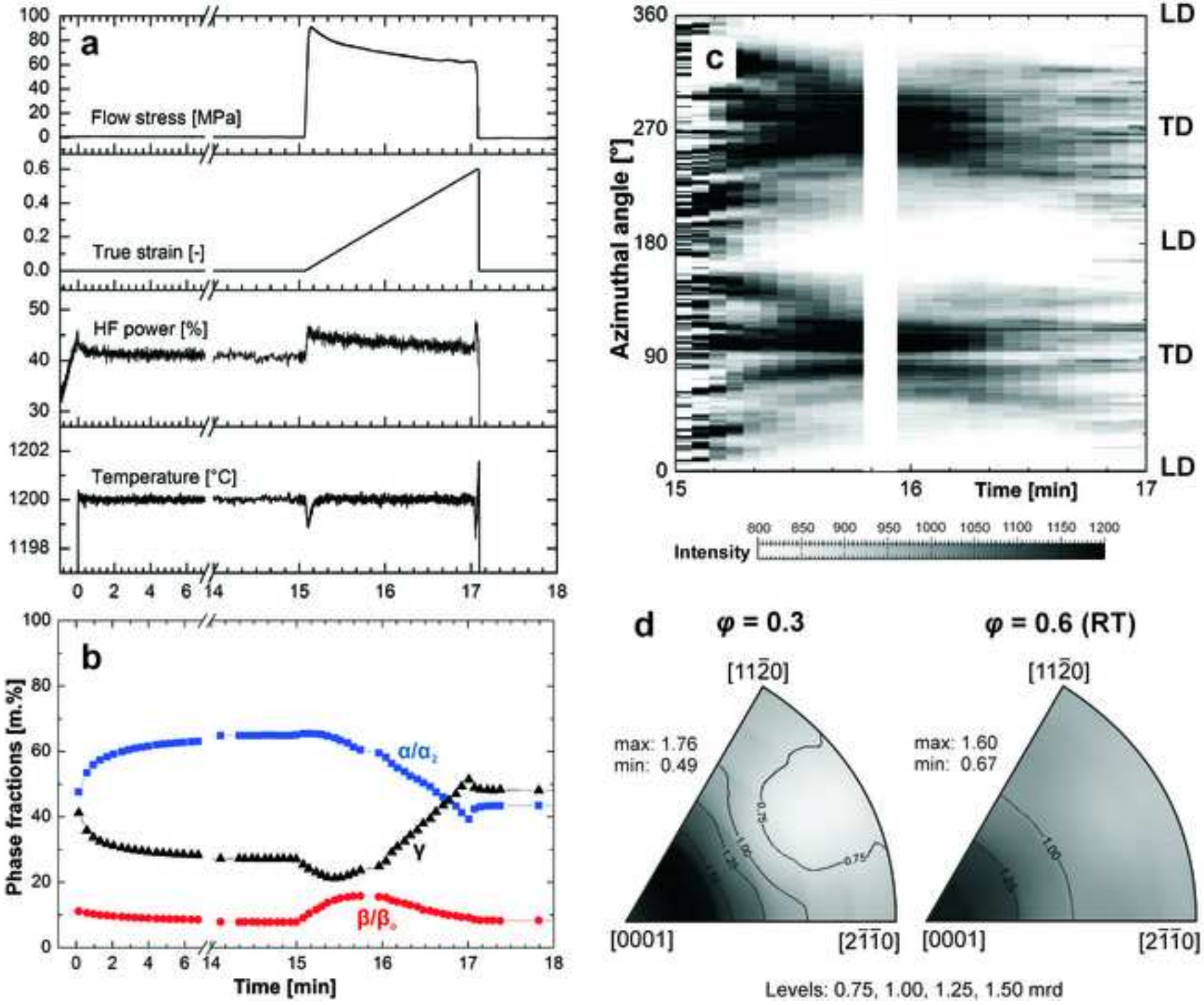

Fig_10

Click here to download high resolution image

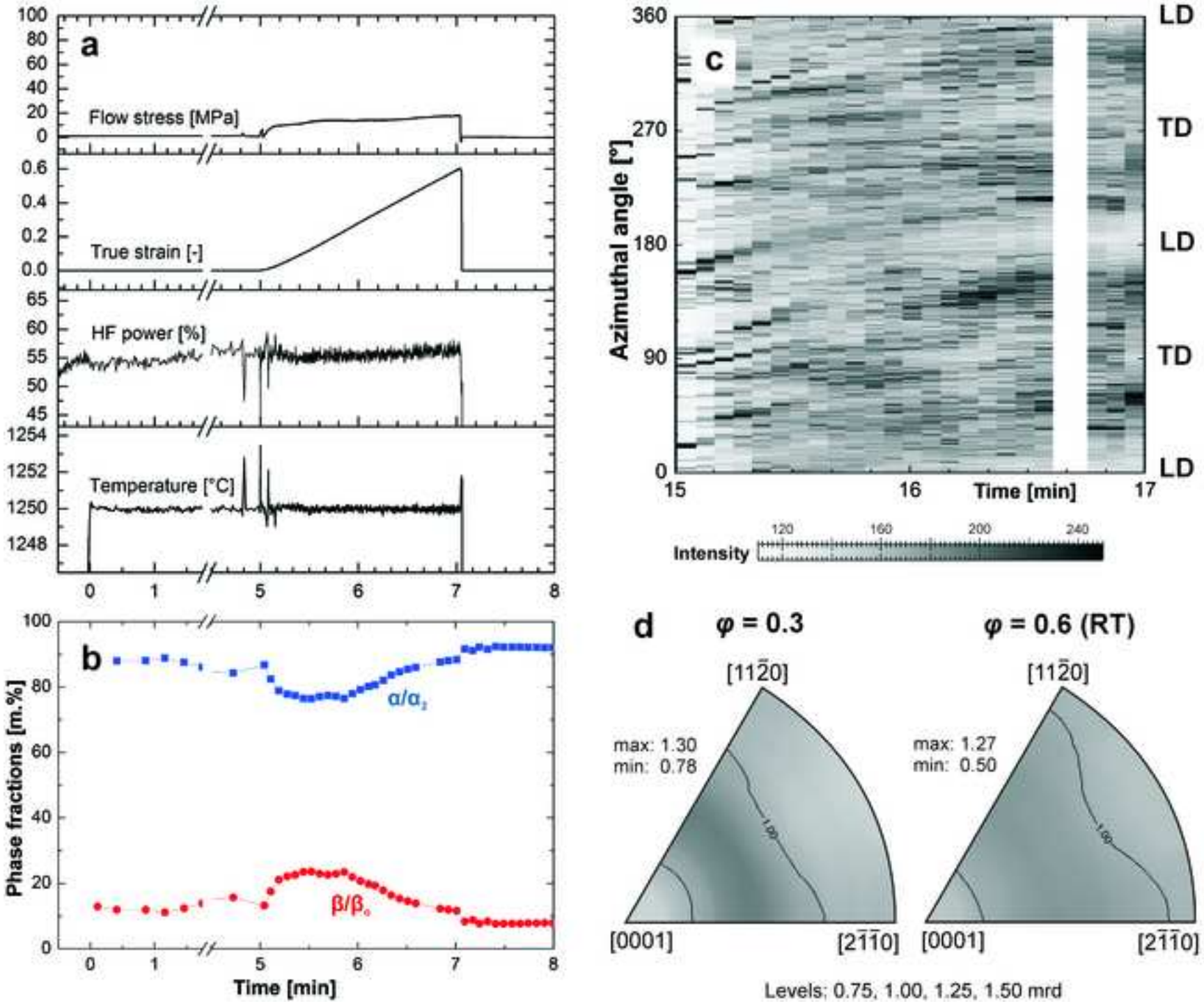

Fig_11

Click here to download high resolution image

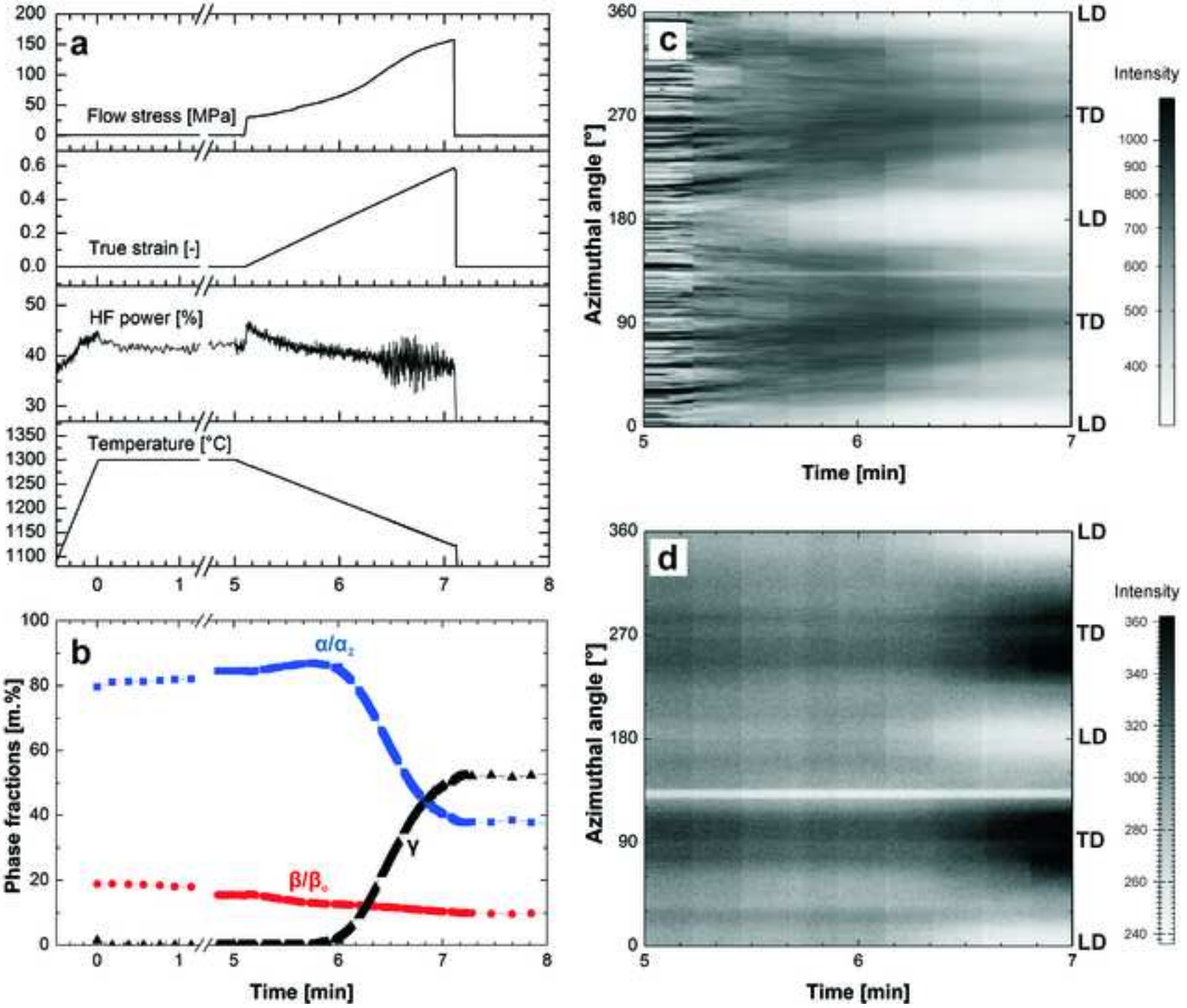

Fig_12

Click here to download high resolution image